Cu_2O/ZnO Heterojunction Solar Cells Fabricated by Magnetron-Sputter Deposition Method Films Using Sintered Ceramics Targets

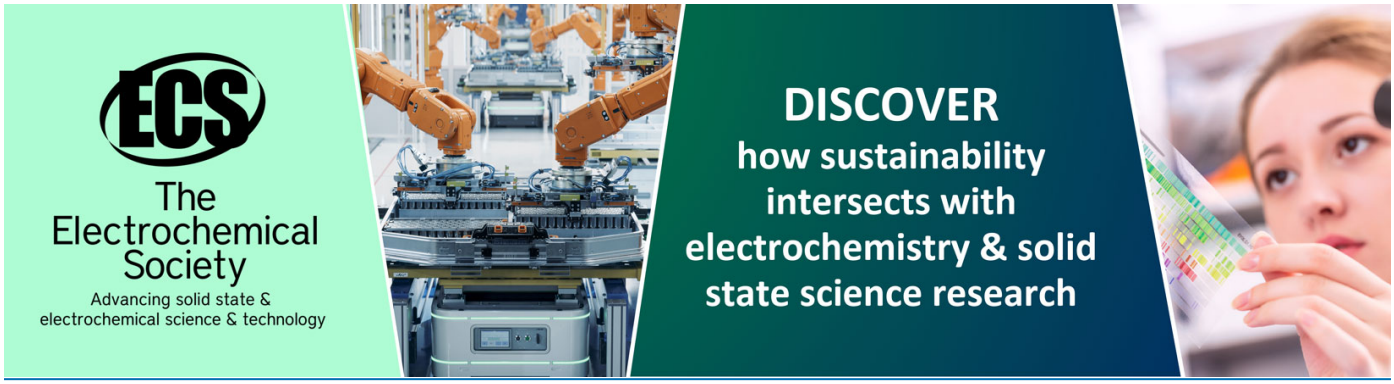

Cu_2O/ZnO Heterojunction Solar Cells Fabricated by Magnetron-Sputter Deposition Method Films Using Sintered Ceramics Targets

S Noda, H Shima and H Akinaga

Innovation Center for Advanced Nanodevices (ICAN), National Institute of Advanced Industrial Science and Technology (AIST), 1-1-1 Central 2, Umezono, Tsukuba, Ibaraki 305-8568, Japan

E-mail: s-noda@aist.go.jp

Abstract. Cu_2O/ZnO heterojucntion solar cells were successfully obtained by a magnetron-sputter deposition method. The Cu_2O thin film was deposited by the method using a sintered Cu_2O ceramics target. Crystalline phases of the films were controlled by adjusting an O_2 flow rate ratio (O_2/(Ar+O_2)) precisely during the sputtering process and Cu_2O single phase polycrystalline films were obtained at room temperature. The Cu_2O films qualities were improved by a rapid thermal annealing for 30 s in an Ar atmosphere of 1 atm. Hall mobility, carrier density, and resistivity of annealed films reached the values of 16.6 $cm^2/V/s$, $3.5x10^{15}$ cm^{-3}, and 107 Ωcm at 600 °C, respectively. The conversion efficiency of the Cu_2O/ZnO heterojucntion solar cell was 0.24 % with the open circuit voltage of 0.69 V.

1. Introduction

Cuprous oxide (Cu_2O) is a promising candidate of an all functional-oxide solar cell material as a p-type active layer because of its photoelectronic properties such as proper energy band gap of 2.1 eV, large optical absorption and high carrier mobility, further, environmentally friendly properties such as non-toxicity, abundance of resource and low material cost. As the solar cell, p-Cu_2O/n-ZnO heterojunction diode structures are most intensively investigated and several kinds of formation methods of the Cu_2O film have been proposed. Thermal oxidization of pure Cu metal sheet at a higher temperature above 1010 °C is one method which can produce the highest quality of Cu_2O film at present [1-4]. Typical Hall mobility (μ_H) is around 100 $cm^2/V/s$ in this method and the highest conversion efficiency (η) of 3.8 % has been obtained using Al-doped ZnO/ZnO/Cu_2O structure recently [1]. Electrodeposition is a low-temperature high-speed method in liquid phase [5-8] and typical μ_H is 1 – 1.8 $cm^2/V/s$. The η value was 0.41 – 0.46 % using Cu_2O/ZnO structure. Recently the highest η of 1.28 % was obtained by optimizing the electrodeosition conditions [5]. This method can utilize ZnO nanopillars and η were improved to 0.88 % by enlarging the interface area [8]. Reactive sputter deposition using pure Cu metal target achieved μ_H of 30 $cm^2/V/s$ at a substrate temperature of 500 °C [9]. The η value of 0.4 % was obtained by this method.

The conversion efficiency is expected to be 18% from the band gap energy of 2.1 eV [10]. However, the current highest efficiency is only 3.8 % even if sufficiently high quality Cu_2O films are used [1]. It is important to realize the precise photovoltaic mechanisms in this system and to estimate

actual conversion limit. Although optical/vibrational properties and intrinsic mechanisms of electrical conduction in the Cu_2O films have been well studied [11], generation and recombination processes of photo-induced carriers in the bulk Cu_2O and at the junction interface have hardly understood yet. And furthermore, optimization of the cell structures is quite difficult because of the difficulty to control the electrical properties of the films. Such circumstances make it difficult to divide the problems existed in the film properties and device structures. Although η is not so improved, the reactive sputter deposition seemed to be most suitable for the applications of the electronic devices. We tried to use sintered ceramics copper oxide targets to lower the deposition temperature to expand application field.

2. Experimental

The Cu_2O films were formed on thermally oxidized Si (oxide), Pt coated oxidized Si (Pt), and synthetic quarts (glass) substrates by an rf magnetron sputtering at room temperature using Ar + O_2 mixture gas system. The oxide and the glass substrates were used to investigate basic characteristics of the films. The Pt substrates were used to fabricate solar cells. The sputtering targets used in this study were commercially available sintered ceramics of Cu_2O (2N) and CuO (3N). Typical gas pressure and rf power density were 0.5 Pa and 3.8 W/cm^2, respectively. The substrates were then annealed by a rapid thermal annealing (RTA) for 30 s in an Ar atmosphere at various temperatures up to 600°C.

Variations in Cu_2O film characteristics according to a change of an O_2 flow rate ratio *Ro* (O_2/(Ar+O_2)) during the sputtering process were investigated in detail. Crystal structure was evaluated by an X-ray diffraction (XRD) for the films deposited on the oxide and the Pt substrates. Optical properties were investigated from a spectral absorption coefficient α measured with an optical absorption spectrometer for the films deposited on the glass substrates. Electrical properties of the films were investigated from resistivity ρ, Hall mobility μ_H, and carrier density n_p. The ρ value was measured with four-point probe and the μ_H and n_p values were obtained by Hall-effect measurement at room temperature for the films on the oxide substrates. Spectral photoconductivity of the films was roughly estimated by measuring electric current between 2.8 mm-gap electrodes formed on the films under illumination. Grain morphology of the Cu_2O films was observed with an atomic force microscope (AFM) in intermittent contact mode for the films on the Pt substrate which are the same structure with the solar cells.

Figure 1 shows a structure of the solar cell fabricated in this study. The cell was basically a heterojunction p-i-n diode device. The p-type Cu_2O layer, an undoped ZnO, and an n^+-type Al doped ZnO (AZO) layer were sputter deposited on the Pt substrates in order. Effective cell area was defined by the area of the ZnO/AZO laminated pattern area as shown in Fig. 1. A number of the cell patterns are formed on the substrate using a shadow mask during the ZnO/AZO depositions. The cell area was varied from 0.0004 to 0.09 cm^2 (0.2 mm square to 3 mm square). The interface between the Cu_2O and the ZnO layers had to be formed successively in vacuo to obtain functioning p/n junction. Therefore, after the continuous deposition of 10 nm-thick ZnO layer on the Cu_2O, the substrates were taken out of the sputtering chamber and proceeded to the RTA treatment. Then the ZnO/AZO patterns were deposited by the magnetron sputtering using the shadow mask. The ZnO and the AZO layers were sputter deposited using sintered ceramics targets of ZnO (4N) and 2%-Al doped ZnO (4N), respectively. The ZnO and the AZO layer were deposited at room temperature and not annealed. The ρ values of the ZnO and the AZO films were 200 k Ωcm and 2.3 m Ωcm, respectively. Electrode pads of Au/Al for the probe contact were deposited by a vacuum evaporation using the shadow mask finally.

Basic properties of the solar cells were investigated from an I-V characteristic and a spectral response (external quantum efficiency: E.Q.E.). Photovoltaic performances of solar cells, that is, closed circuit current (I_{sc}), open circuit voltage (V_{oc}), conversion efficiency (η), fill facter (*FF*) and other values were evaluated with a solar simulator under air-mass (AM) 1.5 illumination.

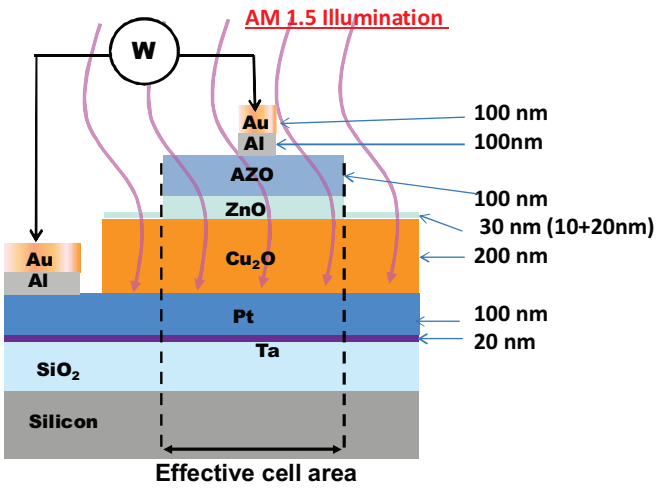

Fig. 1 Solar cell structure fabricated in this study.

3. Results and discussion

3.1. Characteristics of sputter deposited Cu_2O films

Figure 2 shows the XRD spectra of the sputter deposited films using (a) Cu_2O target and (b) CuO target on the oxide substrates at various *Ro* at the room temperature. Since all the films were thin polycrystalline structure and not oriented on the oxide substrates, the XRD measurement was made in a fixed grazing-angle (0.5°) – 2θ (out-of-plane) method. The variations in the film crystallinity were much different by the difference of the target material. In the case of the Cu_2O target (Fig. 2 (a)), the crystalline phase varied significantly by changing *Ro*. At the small *Ro* region below 2.3 %, the films showed Cu_2O crystalline phase only. The Cu_2O crystalline phase was transformed to CuO crystalline phase at large *Ro* region above 8 %. An intermediate phase (Cu_4O_3) was also observed at middle *Ro* region of 3.1 - 4 %. On the other hand, there was little difference in the spectra in the case of the CuO target and only CuO crystalline phase was observed regardless of *Ro* (Fig. 2 (b)). The polycrystalline structures were observed with a scanning electron microscope (SEM). All the films deposited at room temperature had a columnar structure of around 20 nm in diameter.

Figure 3 shows the spectral absorption coefficient of the films on the glass substrates under the same conditions as Fig. 2. In the case of the Cu_2O target-based films (Fig. 3 (a)), the spectrum profile varied significantly with changing *Ro* corresponding to the change of crystalline phase shown in Fig. 2 (a). Reference curves are reported data of single crystal Cu_2O [12] and polycrystalline CuO [13] prepared by a floating-zone (FZ) melting technique [14]. The spectrum profiles of the Cu_2O phase films obtained at small *Ro* region below 1.6 % were almost the same as that of the single crystal except for a small peak shown at low energy region around 1.2 eV. At the large *Ro* region above 2.3 %, the spectrum profile changed gradually to similar profile of the reported CuO with increasing *Ro*. However, the profile did not accord closely with the CuO curve. In the case of the CuO target-based films (Fig. 3 (b)), the spectrum profiles of all the films were very similar with that of the reference CuO curve regardless of *Ro*. It was found that the Cu_2O target was more useful to obtain Cu_2O crystalline phase film and had wider control margin than the CuO target from Figs. 2 and 3. It is considered that the difference in such behaviors is caused by the difference in oxidization reactivity between the two target materials.

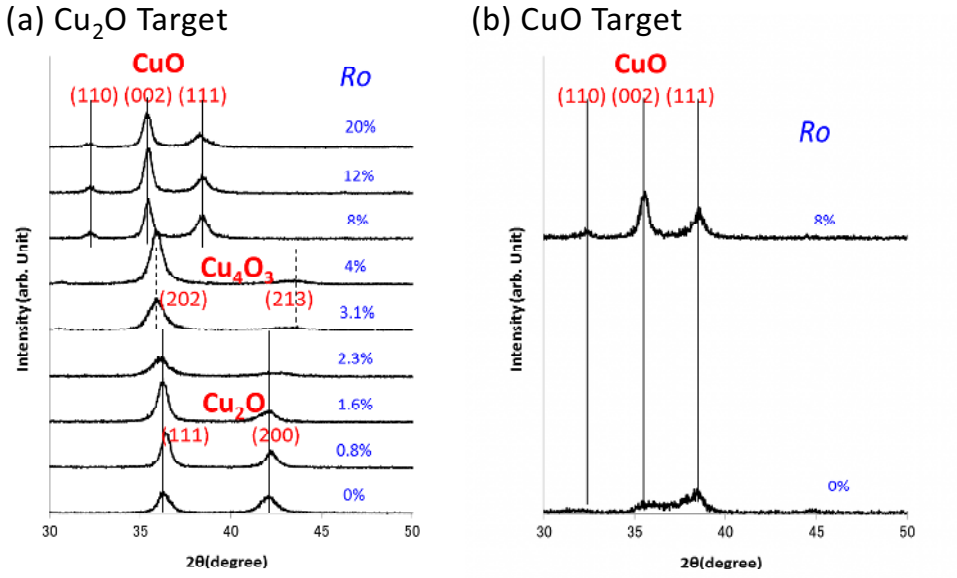

Fig. 2 Variations in crystalline phase of sputter deposited films with changing *Ro* using (a) Cu_2O target and (b) CuO target.

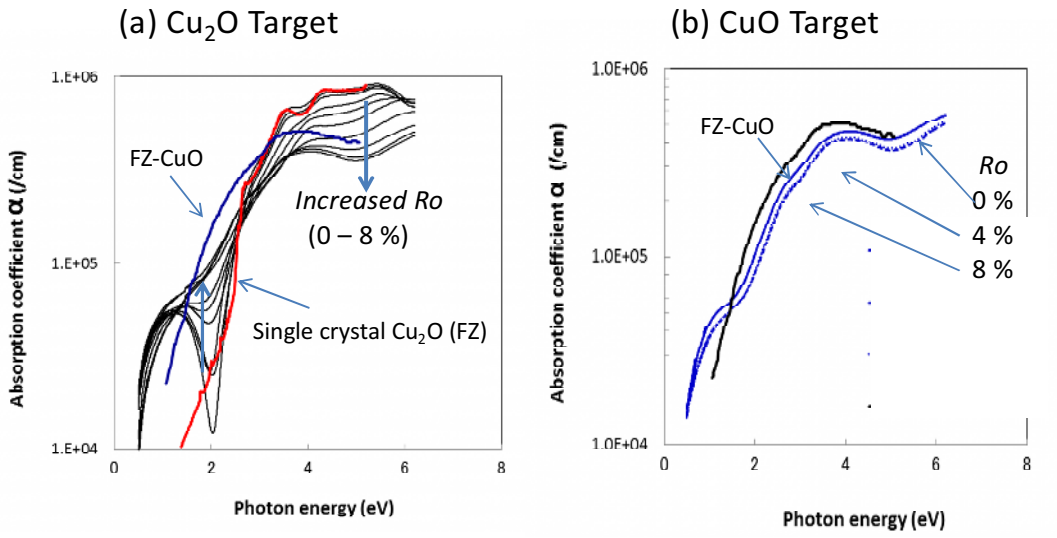

Fig. 3 Variations in optical absorption spectra of sputter deposited films with changing *Ro* using (a) Cu_2O target and (b) CuO target. Reference curves are cited from [12, 13].

The Cu_2O target-based films deposited at room temperature were expected to improve further by heat treatment. Figure 4 shows the XRD spectra of the films deposited at various *Ro* (i.e. of various crystalline phases) before (a) and after (b) the RTA at 600 °C. The spectrum peaks increased sharply and the three crystalline phases of Cu_2O, Cu_4O_3 and CuO were divided into two phases of Cu_2O and CuO by the RTA. It was found that each Cu_2O and CuO polycrystalline film improved itself keeping

its initial crystalline phase and Cu_4O_3 polycrystalline film did not conserve its initial state. The Cu_2O films deposited on the Pt substrate was weekly oriented (111) surface and that was much improved by the RTA differently from the oxide substrates.

The improvement in the Cu_2O film crystallinity by the RTA was also confirmed from optical properties. Figure 5 shows Tauc plot of the absorption coefficient α before (a) and after (b) the RTA. The Cu_2O phase films deposited at small *Ro* region indicated a direct transition and the band gap energy of around 2.6 eV (Fig. 5 (a)). The slope of the absorption edge became steep and a fine structure appeared on the slope after the RTA (Fig. 5 (b)). These two edges were consistent to the E_{0C} ($\Gamma_7^+ \rightarrow \Gamma_8^-$) and E_{0D} ($\Gamma_8^+ \rightarrow \Gamma_8^-$) transition [12] (1s –Yellow band (in-direct; 2.03 – 2.17 eV) does not appear in this plot). It can be said that the Cu_2O phase polycrystalline films were much improved by the RTA.

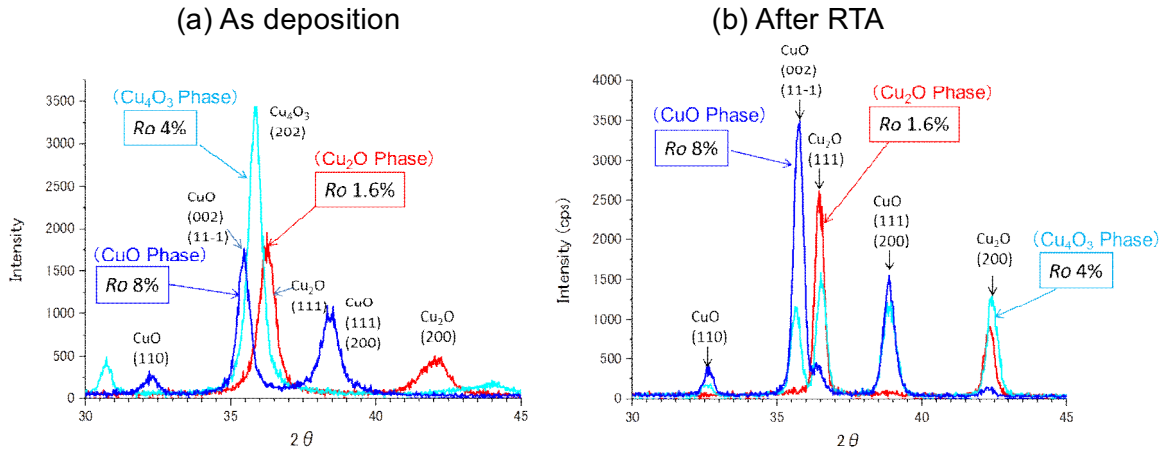

Fig. 4 XRD spectra of Cu_2O target-based films which have several kinds of crystalline phases (a) before and (b) after RTA for 30 s at 600 °C.

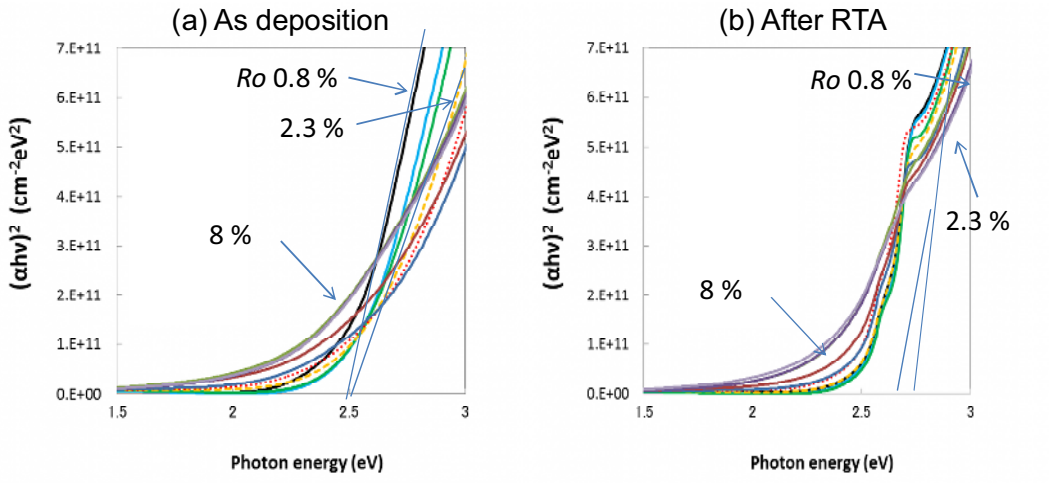

Fig. 5 Tauc plot of absorption coefficient α of Cu_2O target-based films (a) before and (b) after RTA for 30 s at 600 °C.

s at various RTA temperatures observed with the AFM. It was found that the polycrystalline grains began to grow around 400 °C and grew considerably large at 600 °C.

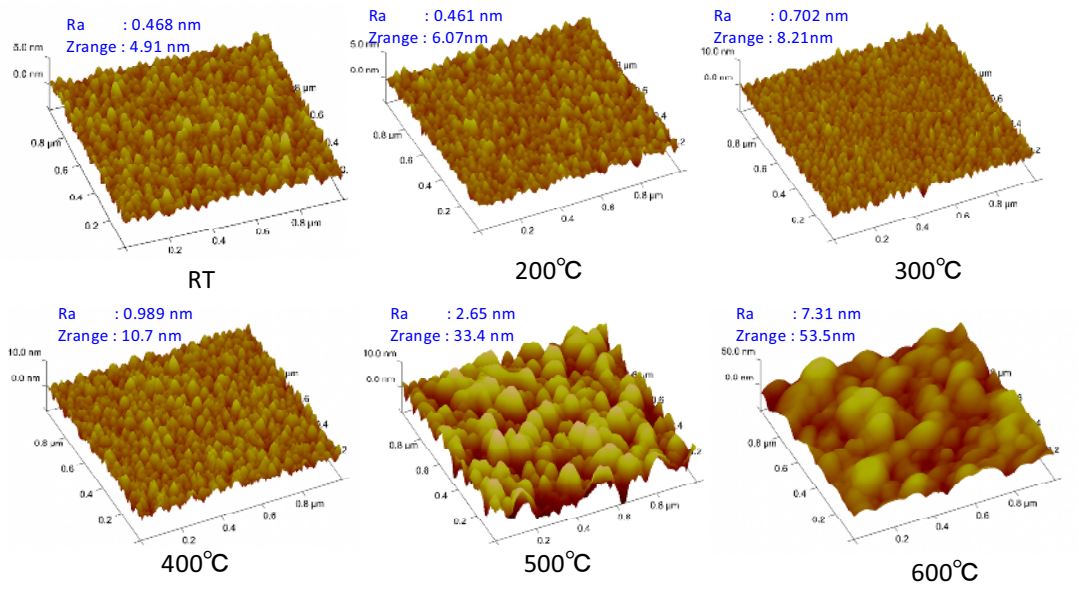

Fig. 6 Surface images of the annealed Cu_2O films on Pt substrates after RTA at various temperatures observed with the AFM.

Figure 7 shows the resistivity ρ of the films without the RTA deposited from the Cu_2O and the CuO targets as a function of *Ro*. Their dependences on *Ro* were significantly different. The ρ value of the Cu_2O target-based films varied complicatedly with increasing *Ro* corresponding to the changes in the crystalline phase as shown in Fig. 2. The ρ value of the Cu_2O phase films (*Ro*: 0 – 2.3%) decreased extremely with a very little increase in *Ro*. Then ρ increased with increasing *Ro* through the Cu_4O_3 phase film region (*Ro*: 2.3 – 8 %). Finally ρ decreased monotonously with increasing *Ro* in the CuO phase film region (*Ro*: 8% –). On the other hand, the CuO target-based films which had only CuO crystalline phase showed a simple dependence on *Ro*. The ρ value decreased monotonously with increasing *Ro*. The decreases of ρ with increasing *Ro*, which are observed in the Cu_2O and CuO phase films are considered to be due to an increase in a density of a Cu vacancy (V_{cu}) mainly. V_{cu} is considered to act as an acceptor in the p-type Cu_2O and CuO. Actually, it was confirmed that the carrier density of the CuO target-based film increased from 9.2 x 10^{16} cm^{-3} to 2.5 x 10^{18} cm^{-3} with increasing *Ro* from 0 to 10 %.

The ρ value of the Cu_2O target-based films varied significantly by RTA. Figure 8 shows the variations of ρ in each crystalline phase as a function of the RTA temperature. The dependences on the temperature were quite different. The ρ value of the highly resistive Cu_2O phase film (*Ro* 0.8 %) decreased largely while that of the low resistive Cu_2O phase film (*Ro* 1.6 %) did not varied so largely with increasing *Ro*. The ρ values of the Cu_4O_3 and CuO phase films increased with increasing *Ro*. Although the reason why ρ of the low resistive Cu_2O film did not changed was unclear, the feature is considered to be useful to control the film properties. Therefore the low resistive Cu_2O phase film (*Ro* 1.6 %) was evaluated for the solar cells.

Figure 9 shows the dependences of μ_H and n_p on the RTA temperature for the low resistive Cu_2O phase film (*Ro* 1.6 %). The μ_H value increased drastically above 400 °C and reached 16.6 $cm^2/V/s$ at 600 °C. At this time, n_p was changed from 3.3x10^{16} to 3.5x10^{15} cm^{-3}. At the RTA temperature region less than 400 °C, reliable μ_H and n_p could not obtained by Hall effect measurement. These dependences are well correspondent with the grain growth shown in Fig. 6.

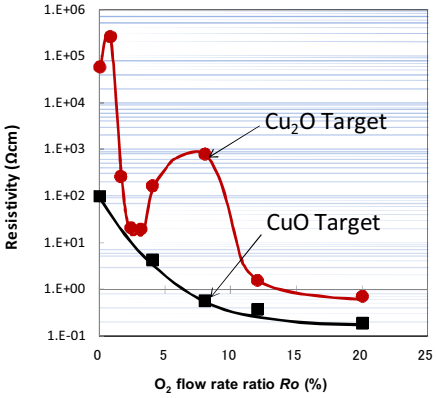

Fig. 7 Dependences of resistivity ρ of Cu_2O target-based film and CuO target-based film on O_2 flow rate ratio *Ro* before RTA.

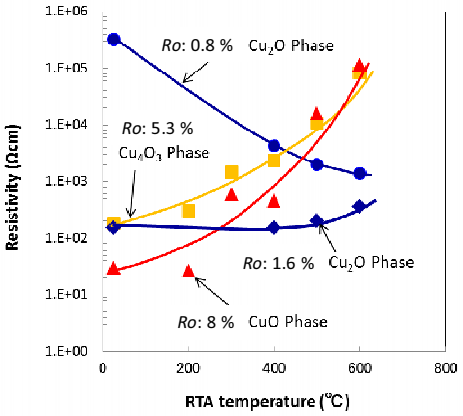

Fig. 8 Dependences of resistivity ρ of Cu_2O target-based films which have various crystalline phases on RTA temperature.

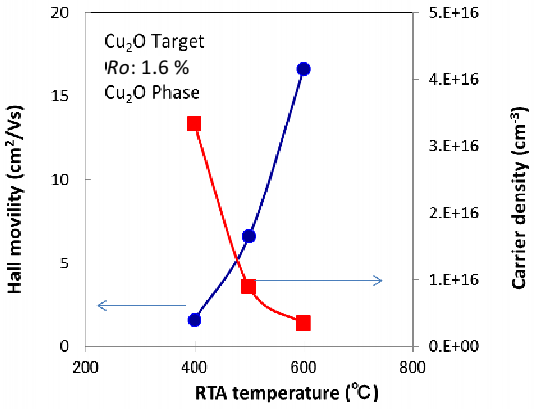

Fig. 9 Dependences of Hall mobility and carrier density on RTA temperature.

3.2. Characteristics of Solar cells

Figure 10 shows the I-V characteristics of the solar cells under a dark condition, which were made by the low resistive Cu_2O phase films (*Ro* 1.6 %) annealed at different temperatures. It was confirmed that a p/n junction was formed successfully even if no RTA was made on the Cu_2O films because good rectification effect was observed regardless of the RTA temperature. An ideality factor n was a little large and increased from 2.0 to 3.8 with increasing the RTA temperature. The relatively large n value is considered to be due to the high series resistance of the Cu_2O layer. Figure 11 shows the I-V curves of the same cells as Fig. 10 under the AM 1.5 illumination. It can be seen that an electric current and a voltage shift were generated by comparing with Fig. 10. The n values became nearly 1.0 in all cells due to generated photoconductivity.

Figure 12 shows the photovoltaic characteristics of the solar cells. The measurement was made for 0.016 cm^2 cells under the AM 1.5 illumination. The performance was improved with increasing the RTA temperature corresponding to the improvement of the film qualities described as above. The I_{sc}, V_{oc}, η and FF values increased to 1.2 mA/cm^2, 0.69 V, 0.24 %, and 0.28, respectively.

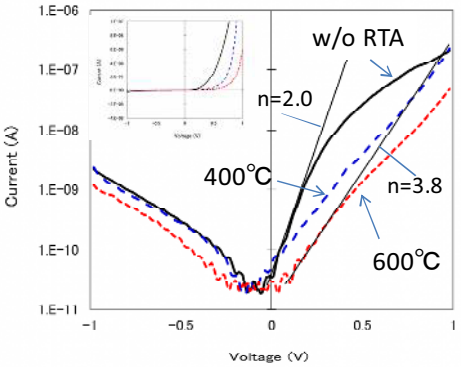

Fig. 10 I-V characteristics of solar cells under dark condition.

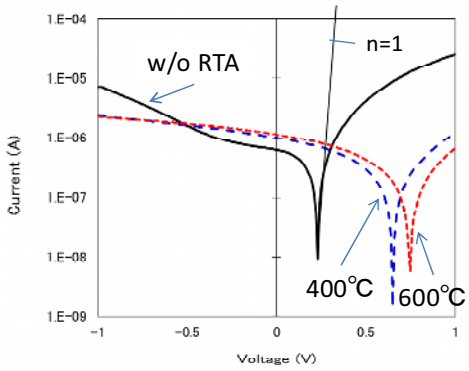

Fig. 11 I-V characteristics of solar cells under AM 1.5 standard illumination.

Fig. 12 Photovoltaic characteristics of solar cells which consist of Cu2O films annealed at various temperatures.

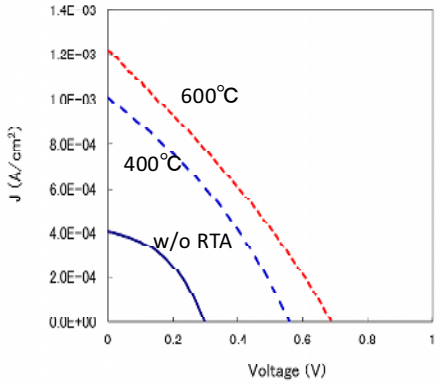

Figure 13 shows the spectral responses of the solar cells. The E.Q.E. improved remarkably by the RTA of 600 °C for the Cu_2O film however the spectral profile was not changed. The efficiency decreased steeply at around the wave length of 400 nm. Figure 14 shows the spectral photocurrent of the Cu_2O films after the RTA of 600 °C. It was observed that the carrier generation was sustained to long-wavelength side around 500 nm which was roughly consistent with the band gap energy of the Cu_2O film obtained in Fig. 5 (b). It was supposed that most of the photogenerated carriers in the wavelength range of 400 – 500 nm were recombined somewhere. Since the power density in the solar light spectrum increases greatly from 400 nm to visible wavelength region, improvement of the efficiency in this range is quite important. As for the short-wavelength side, the photocurrent was not detected in the Cu_2O film but the ZnO film showed the photocurrent instead as shown in the inserted figure in Fig. 14. It was understood that the outer circuit current of the Cu_2O/ZnO solar cell was the sum of the carriers generated in both Cu_2O and ZnO.

Although the efficiency depression in the 400 – 500 nm may be caused by a shortage of the lifetime of the carriers generated far from the interface, there is a possibility that a depletion layer does not exist in the Cu_2O-side, which generates driving field on the generated carriers. To verify this assumption, an effect on the carrier density of the ZnO layer in the p-i-n Solar cell structure was investigated. Precise carrier density control of the oxide semiconductor materials is difficult at present however the carrier density of the ZnO was roughly controlled by *Ro* and the RTA temperature. Figure 15 shows the results. The carrier density of Cu_2O (n_p) and ZnO (n_e) were estimated to be 3.5×10^{15} cm^{-3} and 6.6×10^{18} cm^{-3}, respectively. The efficiency in the 400 – 500 nm region was much improved by controlling a device parameter such as the carrier density. However V_{oc} decreased remarkably from 0.69 V to 0.14 V at the same time due to an increase in the junction leakage. As a result, η was reduced from 0.24 % to 0.047 %. There is a history that the ZnO layer was originally

introduced to prevent the junction leakage and its resistivity must be large. When an ideal interface is realized, η will improve drastically. The controls of the device parameters [15, 16] and interface formation are as important as improving film qualities.

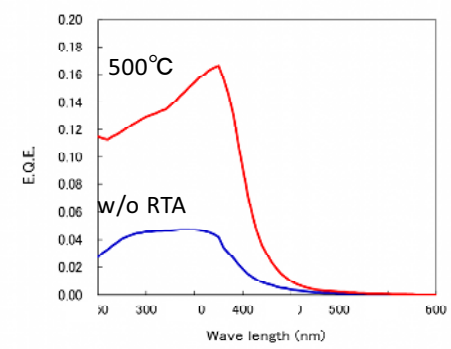

Fig. 13 External quantum efficiency of the solar cells with / without RTA

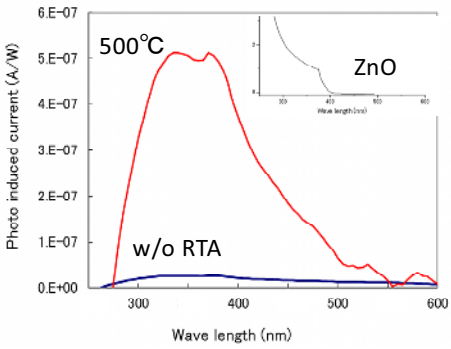

Fig. 14 Photocurrent of Cu_2O phase films. (Inserted figure is that of ZnO film.)

Fig. 15 Improvement in long-wavelength side efficiency by changing carrier density in ZnO layer.

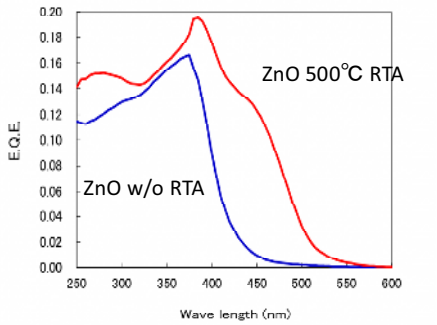

Figure 16 shows cross sectional images of the solar cells (a) without RTA and (b) with 600 °C RTA observed by a transmission electron microscope (TEM). It was observed that the columnar polycrystalline grains were grown from about 20 nm to 200 nm in diameter and the crystallinity was improved. According to this improvement, various characteristics were improved as described above. However there is a trade-off between the film quality and the fabrication results of the solar cells. Actually the yield rate of the quality product decreased with increasing the RTA temperature. The decrease of the yield is considered to be caused by the electrical leakage related to the roughness at the interface. Further modifications such as device structures or fabrication processes are required.

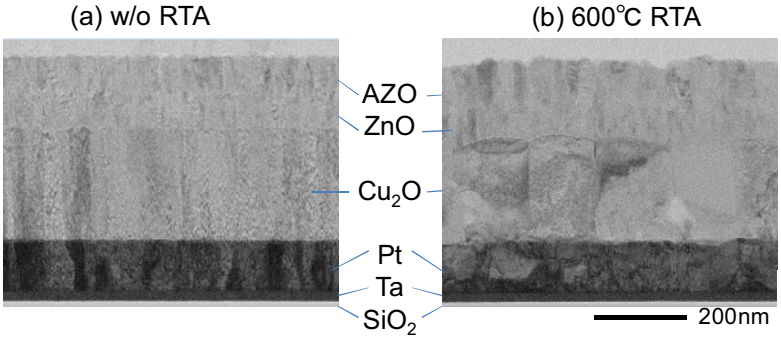

Fig. 16 TEM images of cross sectional view of solar cells (a) before (b) after RTA to 600 °C

4. Conclusion

The magnetron sputter deposition method of the Cu_2O film was investigated by utilizing the Cu_2O and CuO sintered ceramics target in detail for realizing the all functional-oxide solar cells. In the room temperature deposition, the Cu_2O target was more useful to control film properties and three kinds of single polycrystalline phase, Cu_2O, Cu_4O_3 and CuO were selectively formed. The Cu_2O target-based films are improved by the RTA for only 30 s. Especially the Cu_2O phase films were greatly improved in optical and electrical properties by the RTA at 600 °C. The absorption spectra were almost the same as those of the single crystal and the Hall mobility increased to 16.6 cm_2/V/s. By using the sputterd Cu_2O film, Cu_2O/ZnO/AZO solar cells were fabricated. The performance was also improved by the RTA. The conversion efficiency, short circuit current, open circuit voltage and fill factor were 0.24 %, 1.2 mA/cm^2, 0.69V and 0.28, respectively. The spectral response showed that the sensitivity at 400 – 500 nm region was much depressed. It was found that the depression were not due to the Cu_2O properties but were due to the problem of the optimization of device parameters. By the optimization of the device parameters and structure, the conversion efficiency will be expected to improve remarkably.

References

[1] Minami T, Nishi Y, Miyata T and Momoto J 2011 *Appl. Phys. Exp.* **4** 062301
[2] Minami T, Tanaka H, Shimakawa T, Miyata T and Sato H 2004 *Jpn. J. Appl. Phys.* **43** L917
[3] Mittiga A, Salza E, Sarto F, Tucci M and Vasanthi 2006 *Appl. Phys. Lett.* **88** 163502
[4] Tanaka H, Shimakawa T, Miyata T, Sato H and Minami T 2004 *Thin Solid Films* **469** 80
[5] Izaki M, Shinagawa T, Mizuno K, Ida Y, Inaba M and Tasaka A 2007 *J. Phys. D* **40** 3326
[6] Jeong S S, Mittiga A, Salza E Masci A and Passerini S 2008 *Electrochimica Acta* **53** 2226
[7] Hussain S, Cao C, Nabi G, Khan W S, Usman Z and Mahmood T 2011 *Electrochimica Acta* **56** 8342
[8] Cui J and Gibson U J 2010 *J. Phys Chem. C* **114** 6408
[9] Akimoto K, Ishizuka S, Yanagita M, Nawa Y, Paul G K and Sakurai T 2006 *Solar Eenergy* **80** 715
[10] Loferski J J 1956 *J. Appl. Phys.* **27** 777
[11] Shimada H and Masui T 1989 *J. Phys. Soc. Jpn.* **58** 1717
[12] Ito T, Kawashima T, Yamaguchi H, Masumi T and Adachi S 1998 *J. Phys. Soc. Jpn.* **67** 2125
[13] Ito T, Yamaguchi H, Masumi T and Adachi S 1998 *J. Phys. Soc. Jpn.* **67** 3304
[14] Ito T, Yamaguchi H, Okabe K and Masui T 1998 *J. Mater. Sci.* **33** 3555
[15] Liu Y, Turley H K, Tumbleston J R, Samulski E T and Lopez R 2011 *Appl. Phys. Lett.* **98** 162105
[16] Jiang T, Xie T, Zhang Y, Chen L, Peng L, Li H and Wang D 2010 *Phys. Chem. Chem. Phys.* **12** 15476

Acknowledgement

This work was conducted at Nano Processing Facility (NPF) supported by ICAN, AIST. A part of this work was performed at the Center for Integrated Nanotechnologies, a U.S. Department of Energy, Office of Basic Energy Sciences user facility at Los Alamos National Laboratory (Contract DE-AC52-06NA25396) and Sandia National Laboratories (Contract DE-AC04-94AL85000).